Applying two-grid method on unstructured tetrahedra to study fault stability and surface deformation in multiphase geomechanics

Saumik Dana[a], Xiaoxi Zhao[a], Birendra Jha[a]

[a]*Mork Family Department of Chemical Engineering and Materials Science, University of Southern California, Los Angeles, 90007, CA, USA*

Abstract

In an earlier work, we introduced the two-grid method for unstructured tetrahedra applied to staggered solution of coupled flow and poromechanics and demonstrated its accuracy for the benchmark Mandel's problem. In this work, we employ the two-grid method to study surface deformation and fault stability in a field scale carbon storage project.

Keywords: Carbon storage, Multiphase geomechanics, Fault stability, Surface deformation, Unstructured tetrahedral grids

1. Motivation

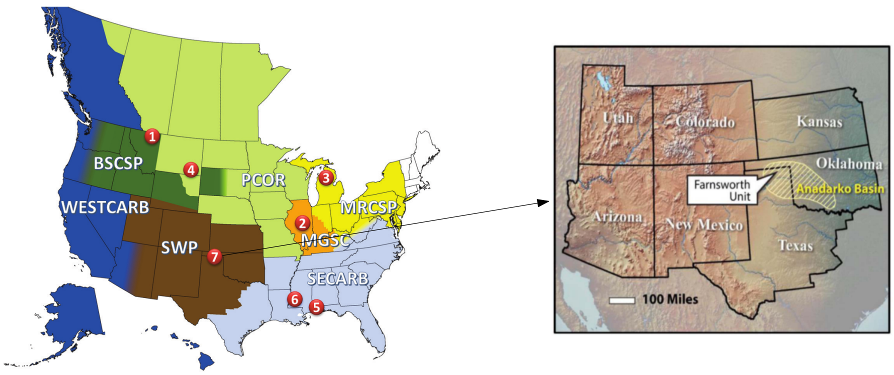

Figure 1: Locations of RCSP large-scale projects. Source: [1]. The Southwest Regional Partnership on Carbon Sequestration (SWP) is one of the seven RCSPs. Geologic extent of the Farnsworth field, Source: [2]

Carbon capture and geologic storage is the separation and capture of CO_2 from emissions of industrial processes, and the transport and permanent storage of the CO_2 in deep underground formations. The U.S. Department of Energy's (DOE) Regional Carbon Sequestration Partnership (RCSP) Initiative was launched in 2003 to advance development and testing of effective CO_2 storage technologies across the United States. This national initiative consists of seven partnerships as shown in Fig. 1. As of September 2016, almost 10 million metric tons of CO_2 have been stored in geologic formations via RCSP large-scale field projects. With the further huge amount of planned CO_2 injection in these large scale projects, the risk of induced seismicity due to fault reactivation is too important to ignore. These seismic risks can be assessed in silico by developing a computationally inexpensive framework with the capability to model multiphase geomechanics and fault stability in a huge domain. These in silico simulations lend to offering guiding protocols for the design of these operations [3, 4, 5, 6, 7, 8, 9, 10, 11, 12, 13, 1, 14]. The major bugbear to developing such a framework is the computationally intractable size of the geomechanical grid no matter which numerical method is used to resolve the coupled system of equations.

Although coupled flow and geomechanics commercial simulators such as Eclipse (Schlumberger) [15] and STARS (CMG) [16] have a long history in practical reservoir management, the calculations associated with storing large amounts of CO_2 for climate mitigation are usually not connected in a uniform framework. The flow simulations require detailed models honouring the flow connectivity of the geological formation, while geomechanical models must account for the mechanical connectivity, including discrete discontinuities such as faults or fractures. The physical processes involved in the creation of the reservoir formations include sedimentation, which generates layers, erosion, which leads to pinch-out or removal of layers, and faulting, which leads to coupling off different types of layers. The result is a complex geometrical model where the physical properties in the model and the grid can not be defined independently. The two critical features in problems involving faults are (1) Fault curvature and intersections must be honored because the fault stresses depend on the fault geometry by definition, and (2) Faults must be extended above and below the production or injection interval i.e. in the overburden and basement to allow modeling of induced seismicity in basement and mechanical integrity failure in caprock. For a compact representation of the physical parameters, reservoir models generally require the use of unstructured grids [17, 18, 19, 20] In lieu of all of the

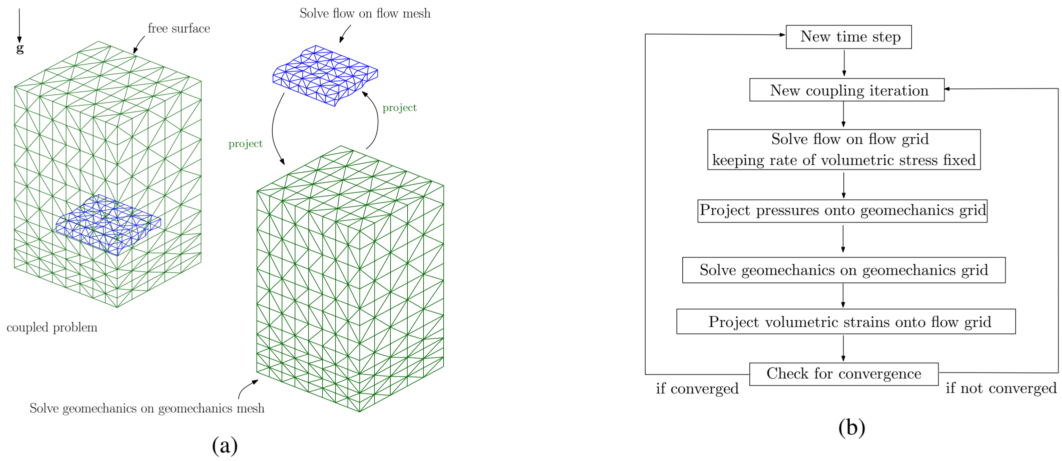

Figure 2: (a) The two-grid method enables the study of induced seismicity in a huge geomechanical domain. Projection operators are used to transfer information from one grid to the other. Source: [21]. (b) Two grid staggered solution algorithm

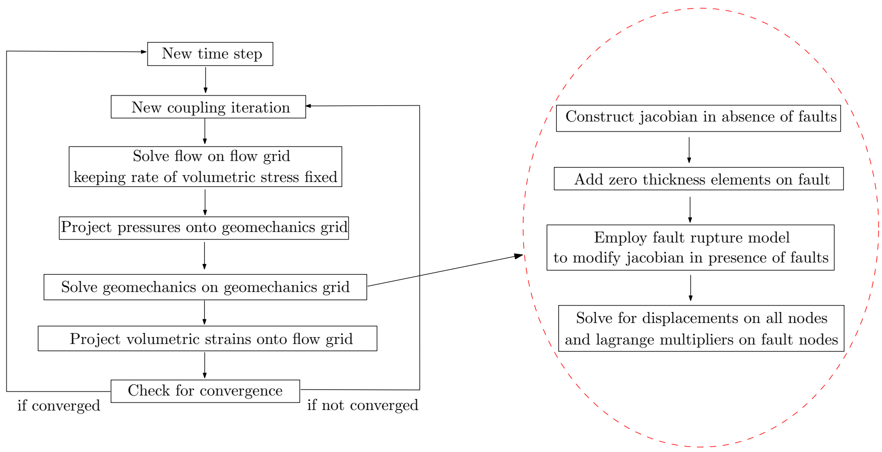

Figure 3: Procedural framework to incorporate faults in the geomechanical system of equations. A brief discussion of the concept of zero thickness elements is provided in Appendix B.

above, we employ a technique which allows for spatial decoupling of the flow and geomechanics domains with the subproblems being resolved on separate unstructured tetrahedral grids (Fig. 2a). As shown in Fig. 2b, the two-grid approach is built on top of a staggered solution algorithm in which the flow and geomechanics subproblems are solved sequentially and iteratively using a fixed stress split iterative scheme [22, 23, 24, 25, 26, 27, 28, 29, 30, 31, 32, 33, 34, 35, 36, 37, 38, 39, 40, 41, 42, 43, 44, 45, 21, 46, 47, 48, 49, 50, 51, 52]. The accuracy of the two-grid method has been demonstrated for the classical Mandel's problem [53, 54] in our earlier work [21]. In the presence of faults though, there is an added set of operations that need to be performed for the solution of the geomechanical problem as shown in Fig. 3.

1.1. Computational framework

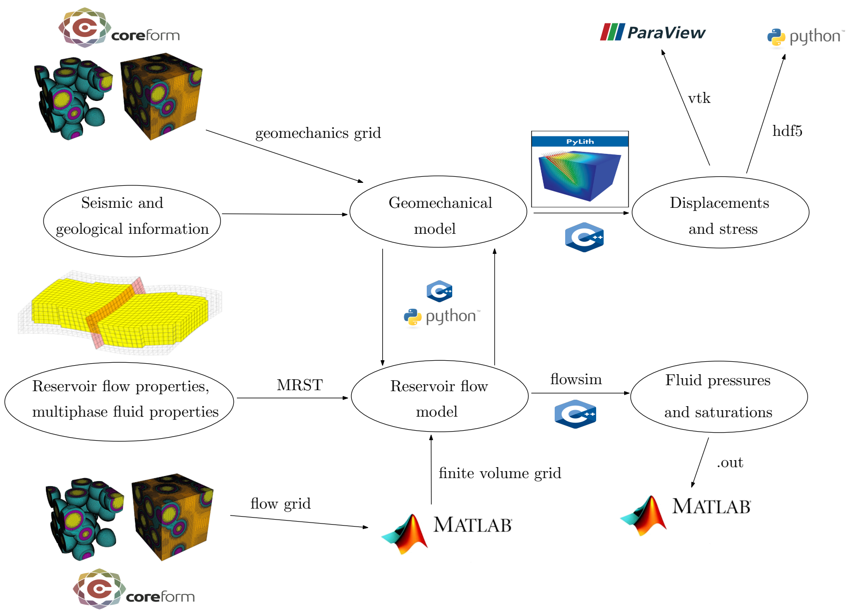

Figure 4: Workflow. Properties like porosity, permeability, fluid density, viscosity, and compressibility are obtained from an older uncoupled model and transferred to the geomechanical model using the Matlab Reservoir Simulation Toolbox [55]. Source: [21]

The governing equations of multiphase poromechanics are laid out in Appendix A. The workflow of the in-house simulator is elucidated in Fig. 4. The flow simulator flowsim is a general purpose, object-oriented, field-scale simulator for multiphase (oil, water, and gas) and multicomponent (e.g. methane, ethane, decane, CO_2, N_2, and water) flow through subsurface. It is capable of handling unstructured grids and complex production and injection scenarios in the field, such as wells perforated at multiple depths and flowing under variable rate and pressure controls. The geomechanics simulator PyLith is a open-source finite element code for the simulation of static and dynamic large-scale deformation problems [56, 57]. It uses an implicit formulation to solve quasi-static problems and an explicit formulation to solve dynamic rupture problems. It allows localized deformation along discrete features, such as faults, and is well integrated with meshing codes, such as CUBIT for both tetrahedral and hexahedral meshes [58].

The details of the space and time discretization and construction of two-grid projection operators are provided in Appendix C. The multiphase flow model is solved using finite volume method whereas the geomechanical equations are solved using finite element method.

2. Numerical simulations

The study area for this work is the CO_2 storage site chosen by the SWP called the Farnsworth Field Unit (FWU). It is a deep structural basin approximately 70,000 square miles in size and primarily located in the northern Texas panhandle and western Oklahoma, and extending into eastern Colorado and western Kansas (see Fig. 1). The field was discovered in 1955 and was unitized in 1963. Secondary recovery commenced in 1964 and CO_2 injection began in December 2010. The field had sequestered approximately 901,556 metric tonnes of CO_2 by June, 2016. The CO_2 for this project is anthropogenically sourced from a fertilizer and an ethanol plant as shown in Fig. 5a. The SWP has a goal of permanently sequestering more than 1 million metric tonnes of CO_2 in this site. A conservative estimate of

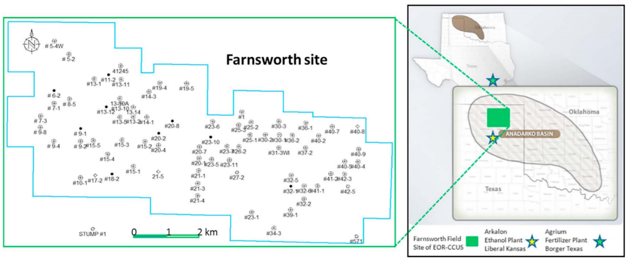

(a)

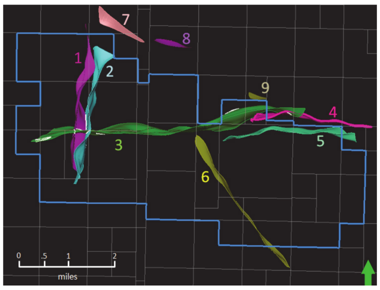

(b)

Figure 5: (a) (Left) The border of FWU and some of the well locations. (Right) CO_2 is anthropogenically sourced from the Arkalon Ethanol Plant in Liberal, Kansas and the Agrium Fertilizer Plant in Borger, Texas. Source: [59, 60]. (b) Faults within or near the Farnsworth Unit (outline shown in blue). Source: [61]

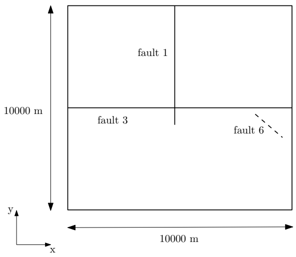

(a) Top view of flow domain, no flow boundary conditions on all boundaries

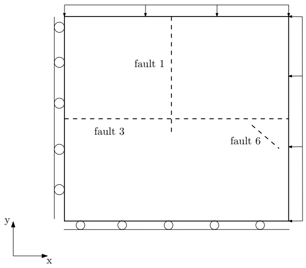

(b) Top view of geomechanics domain

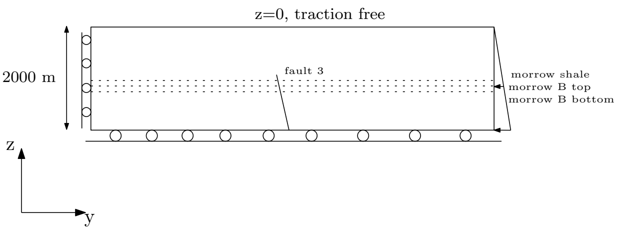

(c) Side view of geomechanics domain

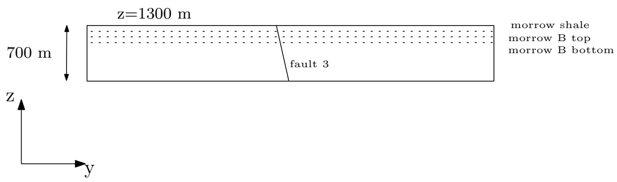

(d) Side view of flow domain

Figure 6: Boundary conditions on flow and geomechanics models

CO_2 storage capacity of the injection zone exceeds 10 million tonnes [59, 62, 63, 64, 65, 66]. As shown in Fig. 5b, nine faults which intersected the Morrow B sandstone reservoir and the limestone caprock were interpreted within the FWU [62, 63, 64, 65, 66]. Because of their locations, Faults 1-3 have the greatest potential for impacting production and carbon sequestration at the FWU [61].

As shown in Fig. 6, we consider faults 1, 3 and 6 in our calculations. Faults 1 and 3 are cutting through the model while fault 6 ends below the reservoir layer. Fault 3 is located near the center of the model and dips toward south with a 6^o angle. No flow boundary condition is imposed on all boundaries of the flow domain. We employ the prescribed fault rupture model (see Appendix B) and prescribe zero slip which means all faults are locked. Our focus in this study is on quantifying the likelihood of failure or the change in mechanical stability of the faults. As shown in Fig. 7a, we employ different grids for flowsim and PyLith to go with our two-grid method. The grids are generated using CUBIT mesh generation software [58]. Since the numerical method employed for the flow model is finite volume instead of finite element, we employ some further processing of the flow grid file to render it for the finite volume calculations.

Reservoir permeability values are obtained by mapping the permeability field of an older model constructed in

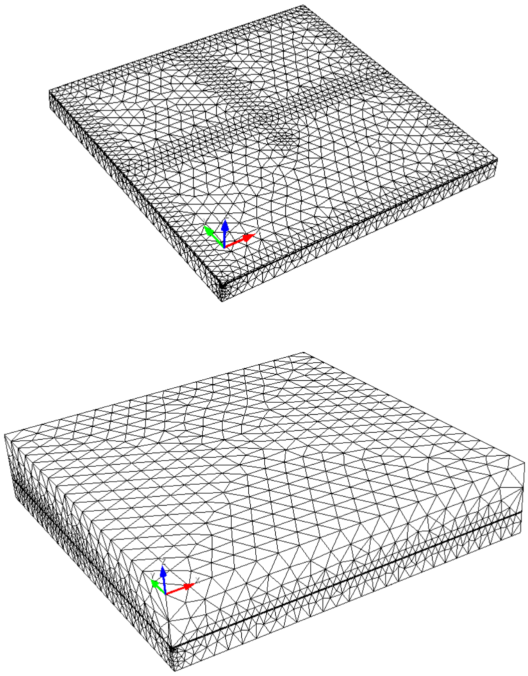

(a) (Above) Flow mesh, 31882 elements (Below) Pylith mesh, 42108 elements

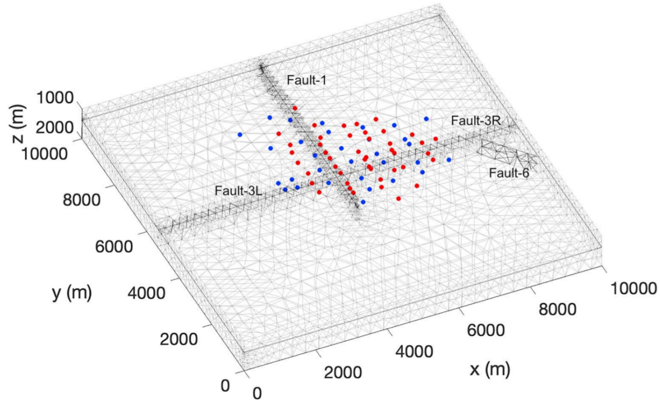

(b) Fault 3 is broken into fault 3L (western part) and fault 3R (eastern part). Injectors are shown with blue dots, and producers are shown with red dots. Source: [60]

Figure 7: Areal extent of both the domains is $10000\,m \times 10000\,m$. The geomechanics domain goes all the way to the free surface $z = 0$ while the flow domain is truncated at $z = -1300\,m$. Both the domains extend upto $z = -2000\,m$

Eclipse on to the coupled geomechanical model [60]. The older model is uncoupled to mechanics, and has been used to track CO_2 migration and oil recovery in FWU [2, 67]. We use a three phase-three component black-oil model [68] to represent the multiphase flow system during flow simulation. The simulation spans approximately 60 years of production and injection from January 1956 to July 2016. As shown in Fig. 7b for the single grid case, there are 76 wells in the field: 45 producers and 31 injectors.

2.1. Observations

The entire simulation runs over roughly 24000 days, but we plot the results at multiple time steps along the way to observe the fault behavior and the effect of the injection/production activity on uplift/subsidence at the free surface. We have plotted the results at the end of 2400 days, which represent the time stamp at around 10 percent of the total simulation time. The surface deformation plot shown in Fig. 8a is counter-intuitive. As the number of producers are more than the number of injectors, we would typically expect subsidence to be observed at the free surface. Instead, we observe uplift at the free surface, which just demonstrates the fact that back-of-the-envelope guesses about ground deformation would be erroneous in most other cases as well. Furthermore, we see three patches of more uplift across the free surface as shown by the red color in Fig. 8a. These observations would be hard to predict without the presence of the simulator that models the overburden and goes all the way to the free surface. Moreover, this capability is critical in cases where multiple forward runs are performed for a subsequent inverse analysis based estimation of the subsurface porosity/permeability fields from ground deformation data obtained from InSAR and/or GPS. We also note that the faults being ‘locked’ does not mean we impose zero normal displacements at the fault nodes. As shown in Fig. 8b, at the bottom of the domain, the faults 1 and 3 have thin streaks of negative z displacement compared to the rest of the botoom of the domain which is held back by the zero displacement boundary condition. The faults being ‘locked’ means that the slip vector at the fault finite elements nodes is assigned a zero magnitude. This means that the fault is not allowed to slide, as the purpose of this study is fault stability and not fault slip. We then plot the z-traction (z being the depth direction) for faults 1 and the western part of fault 3 also refered to as fault 3L. We see that the

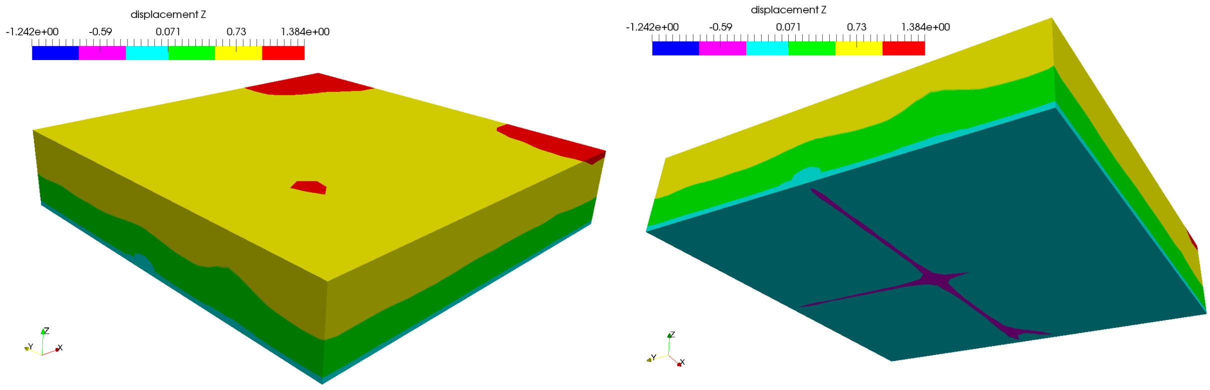

(a) ground deformation

(b) fault kinematics

Figure 8: z-displacement plots after roughly 2400 days

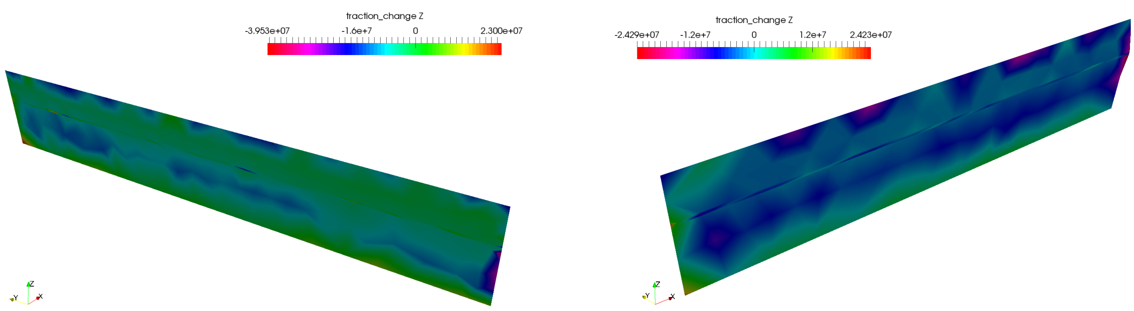

(a) fault 1

(b) fault 3L

Figure 9: z-traction plots after roughly 2400 days

stresses in fault 1 are predominantly compressive which could be a consequence of the pressure of the overlying rock, or it could be a consequence that there are many producers lines up along fault 1 (see Fig. 7b). We do not see as many producers or injectors near fault 3L, which implies the stresses observed on fault 3L could primarily be a consequence of how the overlying rock behaves to the stimulus provided by the wells across the domain. It is important to note though, that the fault 3L does intersect fault 1, and the influence of the fault 1 stress field on fault 3L cannot be ignored as well. It can be hypothesized that the stress field of the predominant fault 1 has an influence on the stress field of fault 3L and vice versa.

3. Continuing work

As we have mentioned, the plots represent the stress field and deformation field at roughly 10 percent of the total simulation time. As and when the further time steps generate more output, we shall plot more results and summarize the observations in a future piece. We shall also compare and contrast the results with the single grid results, albeit the single grid results are plotted on the grid which was truncated at a depth from the free surface. We also intend to have plots for the single grid case where the grid goes all the way to the free surface.

Appendix A. Governing equations of single phase and multiphase poromechanics

Appendix A.1. Balance laws

We use a classical continuum representation in which the fluids and the solid skeleton are viewed as overlapping continua [69, 70]. The governing equations for coupled flow and geomechanics are obtained from conservation of mass and balance of linear momentum. We assume that the deformations are small, that the geomaterial is isotropic, and that the conditions are isothermal.

Let Ω^p be our domain of interest for the geomechanics problem and let $\partial\Omega^p$ be its closed boundary. Under the quasistatic assumption for earth displacements, the governing equation for linear momentum balance of the solid/fluid system can be expressed as

$$\nabla \cdot \boldsymbol{\sigma} + \rho_b \boldsymbol{g} = \mathbf{0}, \tag{A.1}$$

where $\boldsymbol{\sigma}$ is the Cauchy total stress tensor, $\boldsymbol{g}$ is the gravity vector, and $\rho_b = \phi \sum_{\beta}^{n_{\text{phase}}} \rho_\beta S_\beta + (1-\phi)\rho_s$, is the bulk density, ρ_β and S_β are the density and saturation of fluid phase β, ρ_s is the density of the solid phase, ϕ is the true porosity, and n_{phase} is the number of fluid phases. The true porosity is defined as the ratio of the pore volume V_p to the bulk volume V_b in the current (deformed) configuration.
Let Ω^f be our domain of interest for the flow problem and let $\partial\Omega^f$ be its closed boundary. Assuming that the fluids are immiscible, the mass-conservation equation for each phase α is

$$\frac{dm_\alpha}{dt} + \nabla \cdot \boldsymbol{w}_\alpha = \rho_\alpha f_\alpha, \tag{A.2}$$

where the accumulation term dm_α/dt describes the time variation of fluid mass relative to the motion of the solid skeleton, $\boldsymbol{w}_\alpha$ is the mass-flux of fluid phase α relative to the solid skeleton, and f_α is the volumetric source term for phase α. Balance equations (A.1) and (A.2) are coupled by virtue of poromechanics. On one hand, changes in the pore fluid pressure lead to changes in effective stress, and induce deformation of the porous material—such as ground subsidence caused by groundwater withdrawal. On the other hand, deformation of the porous medium affects fluid mass content and fluid pressure.

Appendix A.2. Single-phase poromechanics

For isothermal single-phase flow of a slightly compressible fluid in a poroelastic medium with no stress dependence of permeability, the single-phase fluid mass conservation equation reduces to

$$\frac{dm}{dt} + \nabla \cdot \boldsymbol{w} = \rho_f f, \tag{A.3}$$

where m is the fluid mass content (fluid mass per unit bulk volume of porous medium), ρ_f is the fluid density, $\boldsymbol{w} = \rho_f \boldsymbol{v}$ is the fluid mass flux (fluid mass flow rate per unit area and time), and $\boldsymbol{v}$ is the seepage velocity relative to the deforming skeleton, given by Darcy's law:

$$\boldsymbol{v} = -\frac{\boldsymbol{k}}{\mu}\left(\nabla p - \rho_f \boldsymbol{g}\right), \tag{A.4}$$

where $\boldsymbol{k}$ is the intrinsic permeability tensor, μ is the fluid dynamic viscosity and p is the pore-fluid pressure [69]. It is useful to define the fluid content variation ζ,

$$\zeta := \frac{\delta m}{\rho_{f,0}}, \tag{A.5}$$

where $\delta m = m - m_0$ is the increment in fluid mass content with respect to the initial reference state, and $\rho_{f,0}$ is the reference fluid density. The self-consistent theory of poroelastic behavior proposed by [71] links the changes in total stress and fluid pressure with changes in strain and fluid content. Following [72], the poroelasticity equations can be written in incremental form as

$$\begin{aligned} \delta\boldsymbol{\sigma} &= \boldsymbol{C}_{dr} : \boldsymbol{\varepsilon} - b\delta p \mathbf{1} \\ \zeta &= b\varepsilon_v + \frac{1}{M}\delta p, \end{aligned} \tag{A.6}$$

where $\boldsymbol{C}_{dr}$ is the rank-4 drained elasticity tensor, $\mathbf{1}$ is the rank-2 identity tensor, $\boldsymbol{\varepsilon}$ is the linearized strain tensor, defined as the symmetric gradient of the displacement vector $\boldsymbol{u}$,

$$\boldsymbol{\varepsilon} := \frac{1}{2}\left(\nabla \boldsymbol{u} + \nabla^T \boldsymbol{u}\right), \tag{A.7}$$

and $\varepsilon_v = \mathrm{tr}(\boldsymbol{\varepsilon})$ is the volumetric strain. Note that we use the convention that tensile stress is positive. It is useful to express the strain tensor as the sum of its volumetric and deviatoric components:

$$\boldsymbol{\varepsilon} = \frac{1}{3}\varepsilon_v \mathbf{1} + \boldsymbol{e}, \tag{A.8}$$

from which it follows that the volumetric stress $\sigma_v = \mathrm{tr}(\boldsymbol{\sigma})/3$ satisfies:

$$\delta\sigma_v = K_{dr}\varepsilon_v - b\delta p. \tag{A.9}$$

Equation (A.6) implies that the effective stress in single-phase poroelasticity, responsible for skeleton deformation, is defined in incremental form as

$$\delta\boldsymbol{\sigma}' := \delta\boldsymbol{\sigma} + b\delta p\mathbf{1}. \tag{A.10}$$

Biot's theory of poroelasticity has two coupling coefficients: the Biot modulus M and the Biot coefficient b. They are related to rock and fluid properties as [72]

$$\frac{1}{M} = \phi_0 c_f + \frac{b - \phi_0}{K_s}, \quad b = 1 - \frac{K_{dr}}{K_s}, \tag{A.11}$$

where $c_f = 1/K_f$ is the fluid compressibility, K_f is the bulk modulus of the fluid, K_s is the bulk modulus of the solid grain, and K_{dr} is the drained bulk modulus of the porous medium. To set the stage for the numerical solution strategy of the coupled problem, it is useful to write the fluid mass balance equation (A.3) (the pressure equation) in a way that explicitly recognizes the coupling with mechanical deformation. Equations (A.6) state that the increment in fluid mass content has two components: increment due to expansion of the pore space and increment due to increase in the fluid pressure. Assuming small elastic deformations and applying linearization from the reference state to the current state, we can write Eqs. (A.6) as

$$\boldsymbol{\sigma} - \boldsymbol{\sigma}_0 = \boldsymbol{C}_{dr} : \boldsymbol{\varepsilon} - b\left(p - p_0\right)\mathbf{1}, \tag{A.12}$$

$$\frac{1}{\rho_{f,0}}(m - m_0) = b\varepsilon_v + \frac{1}{M}(p - p_0). \tag{A.13}$$

Substituting Eq. (A.13) into Eq. (A.3), we obtain the fluid mass balance equation in terms of the pressure and the volumetric strain:

$$\frac{1}{M}\frac{\partial p}{\partial t} + b\frac{\partial \varepsilon_v}{\partial t} + \nabla \cdot \boldsymbol{v} = f. \tag{A.14}$$

Linearizing the relation between volumetric total stress and volumetric strain with respect to the reference state,

$$\sigma_v - \sigma_{v,0} = K_{dr}\varepsilon_v - b\left(p - p_0\right), \tag{A.15}$$

allows us to express the change in porosity as the sum of a volumetric stress component and a fluid pressure component. From $m = \rho_f \phi$ and Eq. (A.13),

$$\frac{\rho_f}{\rho_{f,0}}\phi - \phi_0 = \frac{b}{K_{dr}}\left(\sigma_v - \sigma_{v,0}\right) + \left(\frac{b^2}{K_{dr}} + \frac{1}{M}\right)\left(p - p_0\right). \tag{A.16}$$

Using the effective stress equation, Eq. (A.15), we can rewrite Eq. (A.14) in terms of pressure and volumetric total stress:

$$\left(\frac{b^2}{K_{dr}} + \frac{1}{M}\right)\frac{\partial p}{\partial t} + \frac{b}{K_{dr}}\frac{\partial \sigma_v}{\partial t} + \nabla \cdot \boldsymbol{v} = f. \tag{A.17}$$

Appendix A.3. Multiphase poromechanics

In the multiphase or partially saturated fluid system, it is not possible to linearize Eqs. (A.6) around a reference state because [72]:

1. Gases are very compressible,
2. Capillary pressure effects are intrinsically nonlinear, and
3. Phase saturations vary between 0 and 1 and, therefore, a typical problem samples the entire range of nonlinearity.

Therefore, following [72], we use the incremental formulation of poromechanics for multiphase systems, which does not assume physical linearization of total stress from the initial state to the current (deformed) state. Under this formulation, we split the total stress on the porous material into two parts: one that is responsible for deformation of the solid skeleton (the effective stress), and another component that is responsible for changes in the fluid pressures,

$$\delta\boldsymbol{\sigma} = \boldsymbol{C}_{dr} : \delta\boldsymbol{\varepsilon} - \sum_{\beta} b_\beta \delta p_\beta \mathbf{1}, \tag{A.18}$$

where b_β are the Biot coefficients for individual phases such that $\sum_\beta b_\beta = b$, where b is the Biot coefficient of the saturated porous material. It is common to further assume that b_β are proportional to the respective saturations S_β [73, 74, 75]. The effective stress concept allows us to treat a multiphase porous medium as a mechanically equivalent single-phase continuum [76, 77]. The appropriate form of the effective stress equation in a multiphase system is still an active area of research [78, 79, 77, 80, 81, 82]. Here we use the concept of *equivalent pressure* [79] in the effective stress equation (Eq. (A.18)),

$$p_E = \sum_{\beta} S_\beta p_\beta - U, \tag{A.19}$$

where $U = \sum_\beta \int p_\beta dS_\beta$ is the interfacial energy computed from the capillary pressure relations [82]. The equivalent pressure accounts for the interface energy in the free energy of the system, and leads to a thermodynamically consistent and mathematically well-posed description of the multiphase fluid response to the solid deformation [82]. For a system with two phases, the wetting phase w and the non-wetting phase g, the capillary pressure is

$$P_c(S_w) \equiv P_{wg}(S_w) = p_g - p_w, \tag{A.20}$$

and the interfacial energy is $U = \int_{S_w}^{1} P_{wg} dS$. Assuming $b_\beta = bS_\beta$ [73, 74, 75], and using Eq. (A.19) in Eq. (A.18), we obtain the stress-strain relationship for multiphase linear poroelasticity:

$$\delta\boldsymbol{\sigma} = \delta\boldsymbol{\sigma}' - b\delta p_E \mathbf{1}, \quad \delta\boldsymbol{\sigma}' = \boldsymbol{C}_{dr} : \delta\boldsymbol{\varepsilon}. \tag{A.21}$$

In the deformed configuration, the mass of phase α per unit volume of porous medium is

$$m_\alpha = \rho_\alpha S_\alpha \phi(1 + \varepsilon_v). \tag{A.22}$$

Note that, by definition, the sum of all fluid phase saturations satisfies $\sum_\beta^{n_{\text{phase}}} S_\beta \equiv 1$. Extending Eq. (A.13) for multiphase systems [72, 83], we have

$$\left(\frac{dm}{\rho}\right)_\alpha = b_\alpha d\varepsilon_v + \sum_\beta N_{\alpha\beta} dp_\beta, \tag{A.23}$$

where $\boldsymbol{N} = \boldsymbol{M}^{-1}$ is the inverse Biot modulus. In a multiphase system, the Biot modulus is a symmetric positive definite tensor $\boldsymbol{M} = [M_{\alpha\beta}]$, and the Biot coefficient is a vector. To determine the coupling coefficients $N_{\alpha\beta}$ as a function of the primary variables (pressure, saturations, and displacement), and rock and fluid properties, we develop an alternate expression for the differential increment in fluid mass. Using Eq. (A.22),

$$dm_\alpha = d(\rho_\alpha S_\alpha \phi(1 + \varepsilon_v)), \tag{A.24}$$

which can be expanded as

$$\left(\frac{dm}{\rho}\right)_\alpha = \phi \frac{\partial S_\alpha}{\partial P_{\alpha\beta}} dP_{\alpha\beta} + \phi S_\alpha c_\alpha dp_\alpha + \phi S_\alpha d\varepsilon_v + S_\alpha d\phi, \tag{A.25}$$

where $c_\alpha = \frac{1}{\rho_\alpha}\frac{d\rho_\alpha}{dp_\alpha}$ is the compressibility of the fluid phase α, and $\partial S_\alpha / \partial P_{\alpha\beta}$ is the inverse capillary pressure derivative. Above, repeated indices do not imply summation and we have assumed infinitesimal deformations. We can express the increment in porosity, $d\phi$, as a function of the volumetric effective stress, $d\sigma'_v$, to obtain a closed-form expression of Eq. (A.25). Let $V_s = V_b - V_p$ be the volume of the solid matrix, and $d\varepsilon_{sv} = dV_s/V_s = d\sigma_{sv}/K_s$ be the volumetric dilation of the solid matrix, where σ_{sv} is the volumetric matrix stress. From $d\phi = d(V_p/V_b) = \phi(dV_p/V_p - dV_b/V_b)$, we can write the incremental form of strain partition as

$$(1-\phi)d\varepsilon_v = (1-\phi)d\varepsilon_{sv} + d\phi. \tag{A.26}$$

Similarly, the volumetric Cauchy total stress can be partitioned into the volumetric matrix stress and the fluid pressure as

$$d\sigma_v = (1-\phi)d\sigma_{sv} - \phi dp_E. \tag{A.27}$$

Substituting $d\sigma_{sv}$ from Eq. (A.27) into Eq. (A.26), we obtain

$$d\phi = \frac{b-\phi}{K_{dr}}\left(d\sigma'_v + (1-b)dp_E\right). \tag{A.28}$$

Equation (A.28) implies that an increment in porosity is related to increments in volumetric effective stress and fluid pressures, similar to Eq. (A.16) in the single-phase case. Substituting $d\varepsilon_v$ from Eq. (A.21) and $d\phi$ from Eq. (A.28) into Eq. (A.25) allows us to express the increment in the phase mass as a function of the increments in the total volumetric stress and phase pressures. Equating this to Eq. (A.23) yields the desired expressions for the coupling coefficients $N_{\alpha\beta}$, which for a water-gas system are

$$\begin{aligned} N_{gg} &= -\phi\frac{\partial S_w}{\partial P_{wg}} + \phi S_g c_g + S_g^2 N, \\ N_{gw} &= N_{wg} = \phi\frac{\partial S_w}{\partial P_{wg}} + S_g S_w N, \\ N_{ww} &= -\phi\frac{\partial S_w}{\partial P_{wg}} + \phi S_w c_w + S_w^2 N, \end{aligned} \tag{A.29}$$

where $N = (b-\phi)(1-b)/K_{dr}$, and the subscripts w and g denote water and gas phases, respectively. Finally, we obtain the multiphase flow equation for phase α in a poroelastic medium by substituting the two constitutive relations, the effective stress equation, Eq. (A.21), and the fluid mass increment equation, Eq. (A.23), in the mass balance equation, Eq. (A.2):

$$\frac{\partial}{\partial t}\left(\rho_\alpha \sum_\beta \left(N_{\alpha\beta} + \frac{b_\alpha b_\beta}{K_{dr}}\right) p_\beta\right) + \frac{1}{K_{dr}}\frac{\partial}{\partial t}\left(\rho_\alpha b_\alpha \sigma_v\right) + \nabla\cdot\boldsymbol{w}_\alpha = \rho_\alpha f_\alpha,$$
$$\forall\alpha = 1,\ldots,n_{\text{phase}}. \tag{A.30}$$

Because we assume that the fluids are immiscible, the mass-flux of phase α is $\boldsymbol{w}_\alpha = \rho_\alpha \boldsymbol{v}_\alpha$, where we adopt the traditional multiphase-flow extension of Darcy's law [84, 69]:

$$\boldsymbol{v}_\alpha = -\frac{\boldsymbol{k}k^r_\alpha}{\mu_\alpha}(\nabla p_\alpha - \rho_\alpha \boldsymbol{g}), \tag{A.31}$$

where μ_α and k^r_α are the dynamic viscosity and the relative permeability of phase α in presence of other fluid phases.

Appendix B. Fault mechanics

We treat faults as surfaces of discontinuity embedded in the continuum across which displacement is allowed to be discontinuous to recognize the possibility of fault slip [22, 57]. As shown in Fig. B.10, each node on the fault is triplicated to create a "+" node, a "–" node, and a Lagrange node in the middle. The side nodes store the positive side

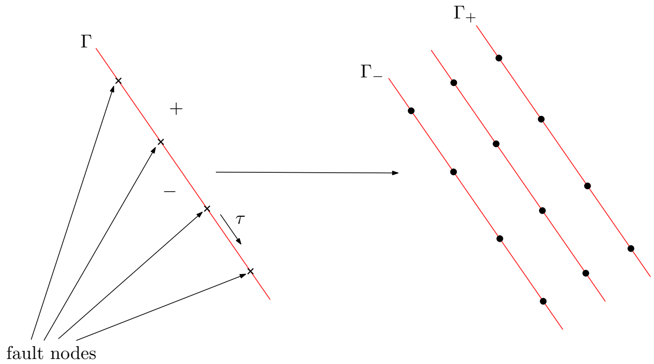

Figure B.10: The two sides of the fault surface, which need not be planar, are designated as the '+' side and the '−' side. Each fault node is triplicated to create a "+" node, a "–" node, and a Lagrange node in the middle

displacement $\mathbf{u}_+$ and the negative side displacement $\mathbf{u}_-$, respectively. All three nodes are physically collocated on the initial grid, so elements representing the fault are zero thickness elements. Slip on the fault is the displacement of the positive side relative to the negative side,

$$(\boldsymbol{u}_+ - \boldsymbol{u}_-) - \boldsymbol{d} = \mathbf{0} \text{ on } \Gamma, \tag{B.1}$$

where $\boldsymbol{d}$ is the fault slip vector. We impose the effective traction on the fault by introducing a Lagrange multiplier, $\boldsymbol{l}$, which is a force per unit area required to satisfy equation B.1. The Lagrange node stores the Lagrange multiplier $\mathbf{l}$ and the fault slip $\mathbf{d}$. The reader is refered to [85, 86, 87] for an understanding of Lagrange multipliers with similar intent in a different context. The Jacobian of the geomechanical system after discretization using finite elements takes the form (see [57, 22] for a more detailed discussion)

$$\begin{bmatrix} \mathbf{K}_{nn} & \mathbf{K}_{nn^+} & \mathbf{K}_{nn^-} & \mathbf{0} \\ \mathbf{K}_{n^+n} & \mathbf{K}_{n^+n^+} & \mathbf{0} & \mathbf{L}_p^T \\ \mathbf{K}_{n^-n} & \mathbf{0} & \mathbf{K}_{n^-n^-} & -\mathbf{L}_p^T \\ \mathbf{0} & \mathbf{L}_p & -\mathbf{L}_p & \mathbf{0} \end{bmatrix}$$

where n denotes degrees of freedom (DOF) not associated with the fault, n^- denotes DOF associated with the negative side of the fault, n^+ denotes DOF associated with the positive side of the fault, and p denotes DOF associated with the Lagrange multipliers. The vector being solved for is

$$\begin{Bmatrix} \mathbf{u}_n \\ \mathbf{u}_{n^+} \\ \mathbf{u}_{n^-} \\ \mathbf{l}_p \end{Bmatrix}$$

Appendix B.1. Prescribed fault rupture

In a prescribed (kinematic) fault rupture, we specify the slip-time history $d(x, y, z, t)$ at every location on the fault surfaces. The vector being solved for is

$$\begin{Bmatrix} \mathbf{u}_n \\ \mathbf{u}_{n^-} \\ \mathbf{l}_p \end{Bmatrix}$$

as the displacements $\mathbf{u}_{n^+}$ on the "+" nodes can be expressed in terms of displacements $\mathbf{u}_{n^-}$ on the "-" nodes using the fault slip. As a result, the number of DOF is considerably reduced. The slip-time history enters into the calculation of the residual as do the Lagrange multipliers, which are available from the current trial solution. In prescribing the slip-time history, we do not specify the initial tractions on the fault surface so the Lagrange multipliers are the change in the tractions on the fault surfaces corresponding to the slip.

Appendix B.2. Spontaneous fault rupture

In contrast to prescribed fault rupture, in spontaneous fault rupture a constitutive model controls the tractions on the fault surface. The shear traction on the fault is computed as

$$\tau = |\mathbf{l} - (\mathbf{l} \cdot \mathbf{n})\mathbf{n}|$$

where $\mathbf{n}$ is the fault normal vector which points from the negative side to the positive side of the fault. The frictional stress τ_f on the fault as

$$\tau_f = \begin{cases} \tau_c - \mu_f \boldsymbol{l} \cdot \boldsymbol{n}, & \boldsymbol{l} \cdot \boldsymbol{n} < 0, \\ \tau_c, & \boldsymbol{l} \cdot \boldsymbol{n} \geq 0, \end{cases} \tag{B.2}$$

where τ_c is the cohesive strength of the fault and μ_f is the coefficient of friction. The coefficient of friction μ_f is a function of the slip magnitude $|\boldsymbol{d}|$, and drops linearly from its static value, μ_s, to its dynamic value, μ_d, over a critical slip distance d_c,

$$\mu_f = \begin{cases} \mu_s - (\mu_s - \mu_d)\frac{|\boldsymbol{d}|}{d_c}, & |\boldsymbol{d}| \leq d_c, \\ \mu_d, & |\boldsymbol{d}| > d_c. \end{cases} \tag{B.3}$$

We use the Mohr-Coulomb theory to define the stability criterion for the fault [88]. When the shear traction on the fault is below the friction stress, $\tau \leq \tau_f$, the fault does not slip. When the shear traction is larger than the friction stress, $\tau > \tau_f$, the contact problem is solved to determine the Lagrange multipliers and slip on the fault, such that the Lagrange multipliers are compatible with the frictional stress [22].

Appendix C. Fully discrete set of equations

Appendix C.1. Fully discrete multiphase flow problem

The flow problem is discretized using the finite volume method on a finer grid than the geomechanics problem, $\Omega^f = \bigcup_{i=1}^{n_f} \Omega_i$ where n_f is the number of flow elements. For simplicity, let us consider two fluid phases, water and gas. Note that in each element, $S_w + S_g \equiv 1$. We integrate the fluid phase mass conservation equation, Eq. (A.30), for each phase over each element i. For the water phase, this yields

$$\begin{aligned} &\frac{\partial}{\partial t} \int_{\Omega_i} \rho_w \left(\left(N_{ww} + N_{wg} + \frac{bb_w}{K_{dr}} \right) p_g - \left(N_{ww} + \frac{b_w^2}{K_{dr}} \right) P_{wg} \right) d\Omega \\ &+ \frac{1}{K_{dr}} \frac{\partial}{\partial t} \int_{\Omega_i} \rho_w b_w \sigma_v d\Omega - \int_{\partial\Omega_i} \boldsymbol{w}_w \cdot \boldsymbol{n}_i d\Gamma = \int_{\Omega_i} \rho_w f_w d\Omega, \end{aligned} \tag{C.1}$$

where we used the capillary pressure relation, $P_{wg} = p_g - p_w$, to eliminate the water phase pressure, the Biot coefficient relation, $b_g + b_w = b$, and integration by parts for the mass-flux term to express it as a surface integral. $\boldsymbol{n}_i$ is the outward normal to the boundary of element i. Similarly, we have a mass balance equation for the gas phase:

$$\begin{aligned} &\frac{\partial}{\partial t} \int_{\Omega_i} \rho_g \left(\left(N_{wg} + N_{gg} + \frac{bb_g}{K_{dr}} \right) p_g - \left(N_{wg} + \frac{b_g b_w}{K_{dr}} \right) P_{wg} \right) d\Omega \\ &+ \frac{1}{K_{dr}} \frac{\partial}{\partial t} \int_{\Omega_i} \rho_g b_g \sigma_v d\Omega - \int_{\partial\Omega_i} \boldsymbol{w}_g \cdot \boldsymbol{n}_i d\Gamma = \int_{\Omega_i} \rho_g f_g d\Omega. \end{aligned} \tag{C.2}$$

We approximate both the pressure and the saturation fields with a piecewise constant interpolation function, φ, such that φ_i takes a constant value of 1 over element i and 0 at all other elements. Phase pressures and saturations are approximated as

$$p_\alpha \approx p_{\alpha,h} = \sum_{i=1}^{n_f} \varphi_i p_{\alpha,i}, \quad S_\alpha \approx S_{\alpha,h} = \sum_{i=1}^{n_f} \varphi_i S_{\alpha,i} \tag{C.3}$$

where the discrete pressures, $p_{\alpha,i}$, and phase saturations, $S_{\alpha,i}$, are located at the center of element i. We can further express the mass flux term as a sum of integral fluxes between element i and its adjacent elements j:

$$\int_{\partial\Omega_i} \boldsymbol{w}_w \cdot \boldsymbol{n}_i d\Gamma = \sum_{j=1}^{n_{\text{face},i}} \int_{\Gamma_{ij}} \boldsymbol{w}_w \cdot \boldsymbol{n}_{ij} d\Gamma = \sum_{j=1}^{n_{\text{face},i}} W_{w,ij}, \tag{C.4}$$

where $n_{\text{face},i}$ is the number of faces of element i, and $\boldsymbol{n}_{ij}$ is the outward normal at the face Γ_{ij}. The inter-element flux of water, $W_{w,ij}$, can be evaluated from Darcy's law (Eq. (A.31)) as a function of the rock and fluid properties, pressures, and saturations of element i and its adjacent elements j, using either a two-point or a multipoint flux approximation [89, 90, 91]. The two-point flux approximation method uses the flow potentials, $\Phi_{w,i} = p_{w,i} - \rho_{w,i} g z_i$ and $\Phi_{w,j} = p_{w,j} - \rho_{w,j} g z_j$, to approximate the flux through interface ij between two neighboring elements as follows:

$$W_{w,ij} = T_{ij} \lambda_{w,ij} \left(\Phi_{w,i} - \Phi_{w,j} \right), \tag{C.5}$$

where z_i and z_j are the centroid depths of the elements (with z-axis pointing downward), $\lambda_{w,ij}$ is the water phase mobility and T_{ij} is the geometric transmissibility of the interface Γ_{ij}. The phase mobility is calculated from upstream cells,

$$\lambda_{w,ij} = \begin{cases} \rho_{w,i} k^r_{w,i} / \mu_{w,i}, & \text{if } \Phi_{w,i} > \Phi_{w,j}, \\ \rho_{w,j} k^r_{w,j} / \mu_{w,j}, & \text{otherwise.} \end{cases} \tag{C.6}$$

The geometric transmissibility is estimated from the harmonic average of the respective element permeabilities and element sizes, $T_{ij} = A_{ij} / (\ell_i / k_i + \ell_j / k_j)$, where A_{ij} is the area of the interface, ℓ_i and ℓ_j are the distances between the centroid of the interface and the centroid of the respective adjacent elements, and k_i and k_j are the element permeabilities, assumed isotropic. After substitution, the semi-discrete water phase mass balance equation is

$$\begin{aligned} 0 = {} & \frac{\partial}{\partial t} \left[V_{b,i} \rho_{w,i} \left(\left(N_{ww} + N_{wg} + \frac{b b_w}{K_{dr}} \right)_i p_{g,i} - \left(N_{ww} + \frac{b_w^2}{K_{dr}} \right)_i P_{wg,i} \right) \right] \\ & + \frac{\partial}{\partial t} \left(\rho_{w,i} \left(\frac{b_w \sigma_v}{K_{dr}} \right)_i V_{b,i} \right) - \sum_{j=1}^{n_{\text{face},i}} W_{w,ij} - \rho_{w,i} f_{w,i} V_{b,i}, \quad \forall i = 1, \ldots, n_f, \end{aligned} \tag{C.7}$$

where subscript i refers to the value at element i. Similarly, we could write the semi-discrete equation for the gas phase:

$$\begin{aligned} 0 = {} & \frac{\partial}{\partial t} \left[V_{b,i} \rho_{g,i} \left(\left(N_{gw} + N_{gg} + \frac{b b_g}{K_{dr}} \right)_i p_{g,i} - \left(N_{gw} + \frac{b_g b_w}{K_{dr}} \right)_i P_{wg,i} \right) \right] \\ & + \frac{\partial}{\partial t} \left(\rho_{g,i} \left(\frac{b_g \sigma_v}{K_{dr}} \right)_i V_{b,i} \right) - \sum_{j=1}^{n_{\text{face},i}} W_{g,ij} - \rho_{g,i} f_{g,i} V_{b,i}, \quad \forall i = 1, \ldots, n_f, \end{aligned} \tag{C.8}$$

The fully discrete system of equations is

$$\begin{aligned} R^{n+1}_{g,i} = {} & \delta_t \left[V_b \rho_g \left(\left(N_{gw} + N_{gg} + \frac{b b_g}{K_{dr}} \right) p_g - \left(N_{gw} + \frac{b_g b_w}{K_{dr}} \right) P_{wg} \right) \right]_i \\ & + \delta_t \left[\rho_g \frac{b_g}{K_{dr}} \sigma_v V_b \right]_i - \sum_{j=1}^{n_{\text{face},i}} W^{n+1}_{g,ij} - \left[\rho^{n+1}_g f^{n+1}_g V_b \right]_i \quad i = 1, \ldots, n_f, \end{aligned} \tag{C.9}$$

$$\begin{aligned} R^{n+1}_{w,i} = {} & \delta_t \left[V_b \rho_w \left(\left(N_{ww} + N_{wg} + \frac{b b_w}{K_{dr}} \right) p_g - \left(N_{ww} + \frac{b_w^2}{K_{dr}} \right) P_{wg} \right) \right]_i \\ & + \delta_t \left[\rho_w \frac{b_w}{K_{dr}} \sigma_v V_b \right]_i - \sum_{j=1}^{n_{\text{face},i}} W^{n+1}_{w,ij} - \left[\rho^{n+1}_w f^{n+1}_w V_b \right]_i \quad i = 1, \ldots, n_f. \end{aligned} \tag{C.10}$$

The global residual vectors are obtained by assembly of the element residual vectors: $\boldsymbol{R}_g = [R_{g,1}, \ldots, R_{g,n_f}]^T$, $\boldsymbol{R}_w = [R_{w,1}, \ldots, R_{w,n_f}]^T$. In vector form, the system of $n_{\text{phase}} \times n_f$ algebraic equations of the flow problem reads:

$$\begin{bmatrix} \boldsymbol{R}_g \\ \boldsymbol{R}_w \end{bmatrix}^{n+1} = \begin{bmatrix} \boldsymbol{0} \\ \boldsymbol{0} \end{bmatrix}, \tag{C.11}$$

which must be solved at every time step for the vector of element gas-phase pressures and water-phase saturations

$$\boldsymbol{P}_g^{n+1} = [p_{g,1}^{n+1}, \ldots, p_{g,n_f}^{n+1}]^T$$
$$\boldsymbol{S}_w^{n+1} = [S_{w,1}^{n+1}, \ldots, S_{w,n_f}^{n+1}]^T$$

The water phase pressure is determined with the help of the capillary pressure relation (Eq. (A.20)), and the gas saturation is determined from the constraint $S_g + S_w \equiv 1$. We solve the linear system of equations of the multiphase flow problem using Newton's method. The correction vector is the solution of the linear system of equations:

$$\begin{bmatrix} \frac{\partial \boldsymbol{R}_g}{\partial \boldsymbol{P}_g} & \frac{\partial \boldsymbol{R}_g}{\partial \boldsymbol{S}_w} \\ \frac{\partial \boldsymbol{R}_w}{\partial \boldsymbol{P}_g} & \frac{\partial \boldsymbol{R}_w}{\partial \boldsymbol{S}_w} \end{bmatrix}^{(k)} \begin{bmatrix} \delta \boldsymbol{P}_g \\ \delta \boldsymbol{S}_w \end{bmatrix}^{(k)} = - \begin{bmatrix} \boldsymbol{R}_g \\ \boldsymbol{R}_w \end{bmatrix}^{(k)}, \tag{C.12}$$

where the partial derivatives of the residuals are evaluated using the constitutive equations (Eq. (A.29) and Eq. (A.31)) that relate rock and fluid properties to the fluid pressures and saturations. Flow problem is solved using the SAMG multigrid pre- conditioner [92, 93].

Appendix C.2. Fully discrete geomechanics problem

Find $(\boldsymbol{u}, \boldsymbol{l})$ belonging to appropriate functional spaces satisfying the essential boundary conditions ($\boldsymbol{u} = \bar{\boldsymbol{u}}$ on Γ_u) such that

$$\int_{\Omega^p} \nabla^s \boldsymbol{\eta} : (\boldsymbol{\sigma}' - b p_E \boldsymbol{1}) d\Omega^p + \int_{\Gamma_{f+}} \boldsymbol{\eta} \cdot (\boldsymbol{l} - b p_f \boldsymbol{n}) d\Gamma - \int_{\Gamma_{f-}} \boldsymbol{\eta} \cdot (\boldsymbol{l} - b p_f \boldsymbol{n}) d\Gamma - \int_{\Omega^p} \boldsymbol{\eta} \cdot \rho_b \boldsymbol{g} d\Omega^p - \int_{\Gamma_\sigma} \boldsymbol{\eta} \cdot \bar{\boldsymbol{t}} d\Gamma = \boldsymbol{0}, \tag{C.13}$$

$$\int_{\Gamma_{f+}} \boldsymbol{\eta} \cdot \boldsymbol{u}_+ d\Gamma - \int_{\Gamma_{f-}} \boldsymbol{\eta} \cdot \boldsymbol{u}_- d\Gamma - \int_{\Gamma_f} \boldsymbol{\eta} \cdot \boldsymbol{d} d\Gamma = \boldsymbol{0}, \tag{C.14}$$

for all test functions $\boldsymbol{\eta}$ ($n_{\text{dim}} \times 1$ vector) belonging to the appropriate functional space satisfying $\boldsymbol{\eta} = \boldsymbol{0}$ on Γ_u. Here, we used the multiphase effective stress equation (Eq. (A.21)), p_E is the equivalent pressure (Eq. (A.19)), p_f is the fault pressure, and ρ_b is the bulk density, all of which depend on the phase pressures and saturations, and, therefore, on the solution of the flow problem.

Let the domain be partitioned into non-overlapping elements (grid blocks), $\Omega^p = \bigcup_{j=1}^{n_{\text{elem}}} \Omega_j$ where n_{elem} is the number of geomechanics elements. For the remainder of this section, we shall use the variable Ω instead of Ω^p for the sake of notational convenience. A fault is treated as an interior boundary with its domain, Γ_f, partitioned into non-overlapping fault elements, $\Gamma_f = \bigcup_{j=1}^{n_{f,\text{elem}}} \Gamma_{f,j}$, where the subscript f indicates variables associated with a fault. The displacement, the Lagrange multiplier, and the slip fields are approximated as follows:

$$\boldsymbol{u} \approx \boldsymbol{u}_h = \sum_{b=1}^{n_{\text{node}}} \eta_b \boldsymbol{U}_b, \quad \boldsymbol{l} \approx \boldsymbol{l}_h = \sum_{\bar{b}=1}^{n_{f,\text{node}}} \eta_{\bar{b}} \boldsymbol{L}_{\bar{b}}, \quad \boldsymbol{d} \approx \boldsymbol{d}_h = \sum_{\bar{b}=1}^{n_{f,\text{node}}} \eta_{\bar{b}} \boldsymbol{D}_{\bar{b}}, \tag{C.15}$$

where subscript h indicates the finite element approximation, n_{node} is the number of displacement nodes (including the duplicated nodes at the fault elements, and $n_{f,\text{node}}$ is the number of Lagrange nodes. $\boldsymbol{U}_b$ is the $n_{\text{dim}} \times 1$ vector of nodal displacements for node b in the domain coordinate system, $\boldsymbol{U}_b = (U_{b,x}, U_{b,y}, U_{b,z})$. $\boldsymbol{L}_{\bar{b}}$ and $\boldsymbol{D}_{\bar{b}}$ are the $n_{\text{dim}} \times 1$ Lagrange multiplier and slip vectors at Lagrange node $\bar{b}$ of the fault, and they are in the fault coordinate system (left-lateral, reverse, and opening, respectively: $\boldsymbol{L}_{\bar{b}} = (L_{\bar{b},1}, L_{\bar{b},2}, L_{\bar{b},3})$ and $\boldsymbol{D}_{\bar{b}} = (D_{\bar{b},1}, D_{\bar{b},2}, D_{\bar{b},3})$.

The interpolation functions, η_b and $\eta_{\bar{b}}$, are the usual C^0-continuous isoparametric functions, such that they take a value of 1 at the respective nodes, and 0 at all other nodes [94]. In a Galerkin method, the test functions are chosen to be equal to the interpolation functions.

After substitution of the finite element approximations into the weak form of the problem (Eqs. (C.13)–(C.14)), we obtain the discrete equations in residual form at all displacement nodes a and all Lagrange nodes $\bar{a}$:

$$
\begin{aligned}
\mathbf{0} = & \int_{\Omega} \boldsymbol{B}_a^T(\boldsymbol{\sigma}'_h - bp_{E,h}\mathbf{1})d\Omega + \int_{\Gamma_{f+}} \boldsymbol{\eta}_a^T(\boldsymbol{l}_h - bp_{f,h}\boldsymbol{n})d\Gamma - \int_{\Gamma_{f-}} \boldsymbol{\eta}_a^T(\boldsymbol{l}_h - bp_{f,h}\boldsymbol{n})d\Gamma \\
& - \int_{\Omega} \boldsymbol{\eta}_a^T\rho_{b,h}\boldsymbol{g}d\Omega - \int_{\Gamma_\sigma} \boldsymbol{\eta}_a^T\bar{\boldsymbol{t}}d\Gamma \quad \forall a = 1,\ldots,n_{\text{node}}, \qquad \text{(C.16)}\\
\mathbf{0} = & \int_{\Gamma_{f+}} \boldsymbol{\eta}_{\bar{a}}^T\boldsymbol{u}_{h_+}d\Gamma - \int_{\Gamma_{f-}} \boldsymbol{\eta}_{\bar{a}}^T\boldsymbol{u}_{h_-}d\Gamma - \int_{\Gamma_f} \boldsymbol{\eta}_{\bar{a}}^T\boldsymbol{d}_h d\Gamma \quad \forall \bar{a} = 1,\ldots,n_{f,\text{node}}, \qquad \text{(C.17)}
\end{aligned}
$$

where we have defined the nodal matrices for the shape function

$$
\boldsymbol{\eta}_a = \begin{bmatrix} \eta_a & 0 & 0 \\ 0 & \eta_a & 0 \\ 0 & 0 & \eta_a \end{bmatrix}. \qquad \text{(C.18)}
$$

and its symmetric gradient

$$
\boldsymbol{B}_a = \begin{bmatrix} \partial_x\eta_a & 0 & 0 \\ 0 & \partial_y\eta_a & 0 \\ 0 & 0 & \partial_z\eta_a \\ \partial_y\eta_a & \partial_x\eta_a & 0 \\ 0 & \partial_z\eta_a & \partial_y\eta_a \\ \partial_z\eta_a & 0 & \partial_x\eta_a \end{bmatrix}, \qquad \text{(C.19)}
$$

corresponding to the compact engineering notation for stress and strain inside an element,

$$
\begin{aligned}
\boldsymbol{\sigma}'_h &= [\sigma'_{h,xx}, \sigma'_{h,yy}, \sigma'_{h,zz}, \sigma'_{h,xy}, \sigma'_{h,yz}, \sigma'_{h,xz}]^T, \\
\boldsymbol{\varepsilon}_h &= [\varepsilon_{h,xx}, \varepsilon_{h,yy}, \varepsilon_{h,zz}, 2\varepsilon_{h,xy}, 2\varepsilon_{h,yz}, 2\varepsilon_{h,xz}]^T
\end{aligned}
$$

respectively [94]. The identity tensor in compact notation is $\mathbf{1} = [1,1,1,0,0,0]^T$. Equation (C.16) results in $n_{\text{dim}} \times n_{\text{node}}$ equations, and Eq. (C.17) results in $n_{\text{dim}} n_{f,\text{node}}$ equations. Since we use the prescribed fault rupture model, $\delta \boldsymbol{D}_{\bar{a}}$ is prescribed at all fault nodes. The fully discrete system of equations is

$$
\begin{aligned}
\boldsymbol{R}_{u,a}^{n+1} = & \int_{\Omega} \boldsymbol{B}_a^T(\boldsymbol{\sigma}'^{n+1}_h - bp_{E,h}^{n+1}\mathbf{1})d\Omega + \int_{\Gamma_{f+}} \boldsymbol{\eta}_a^T(\boldsymbol{l}_h^{n+1} - bp_{f,h}^{n+1}\boldsymbol{n})d\Gamma \\
& - \int_{\Gamma_{f-}} \boldsymbol{\eta}_a^T(\boldsymbol{l}_h^{n+1} - bp_{f,h}^{n+1}\boldsymbol{n})d\Gamma - \int_{\Omega} \boldsymbol{\eta}_a^T\rho_{b,h}^{n+1}\boldsymbol{g}d\Omega - \int_{\Gamma_\sigma} \boldsymbol{\eta}_a^T\bar{\boldsymbol{t}}d\Gamma = \mathbf{0} \\
& \forall a = 1,\ldots,n_{\text{node}}, \qquad \text{(C.20)}\\
\boldsymbol{R}_{l,\bar{a}}^{n+1} = & \int_{\Gamma_{f+}} \boldsymbol{\eta}_{\bar{a}}^T\boldsymbol{u}_{h_+}^{n+1}d\Gamma - \int_{\Gamma_{f-}} \boldsymbol{\eta}_{\bar{a}}^T\boldsymbol{u}_{h_-}^{n+1}d\Gamma - \int_{\Gamma_f} \boldsymbol{\eta}_{\bar{a}}^T\boldsymbol{d}_h^{n+1}d\Gamma = \mathbf{0} \quad \forall \bar{a} = 1,\ldots,n_{f,\text{node}}, \qquad \text{(C.21)}
\end{aligned}
$$

The global residual vectors are obtained by assembly of the nodal residual vectors: $\boldsymbol{R}_u = [\boldsymbol{R}_{u,1},\ldots,\boldsymbol{R}_{u,n_{\text{node}}}]^T$, $\boldsymbol{R}_l = [\boldsymbol{R}_{l,1},\ldots,\boldsymbol{R}_{l,n_{\text{f,node}}}]^T$. In vector form, the system of $(n_{\text{dim}} n_{\text{node}} + n_{\text{dim}} n_{f,\text{node}})$ algebraic equations of the mechanical problem reads:

$$
\begin{bmatrix} \boldsymbol{R}_u \\ \boldsymbol{R}_l \end{bmatrix}^{n+1} = \begin{bmatrix} \mathbf{0} \\ \mathbf{0} \end{bmatrix}, \qquad \text{(C.22)}
$$

which needs to be solved for the displacements $\boldsymbol{U}^{n+1} = [\boldsymbol{U}_1^{n+1},\ldots,\boldsymbol{U}_{n_{\text{node}}}^{n+1}]^T$ at the displacement nodes, and the Lagrange multipliers $\boldsymbol{L}^{n+1} = [\boldsymbol{L}_1^{n+1},\ldots,\boldsymbol{L}_{n_{\text{f,node}}}^{n+1}]^T$ at the Lagrange nodes, subject to the constraint (Eq. (B.1)) at every time step. We solve the linear systems of equations of the mechanical problem using Newton's method. Given an approximation $[\boldsymbol{U}^{n+1}, \boldsymbol{L}^{n+1}]^{(k)}$ to the solution at t_{n+1}, an improved solution is obtained as

$$
[\boldsymbol{U}^{n+1}, \boldsymbol{L}^{n+1}]^{(k+1)} = [\boldsymbol{U}^{n+1}, \boldsymbol{L}^{n+1}]^{(k)} + [\delta\boldsymbol{U}^{n+1}, \delta\boldsymbol{L}^{n+1}]^{(k)}
$$

where the correction vector is the solution to the system of linear equations (removing the explicit reference to the time level $n+1$):

$$\begin{bmatrix} \boldsymbol{K} & \boldsymbol{C}^T \\ \boldsymbol{C} & \boldsymbol{0} \end{bmatrix}^{(k)} \begin{bmatrix} \delta \boldsymbol{U} \\ \delta \boldsymbol{L} \end{bmatrix}^{(k)} = - \begin{bmatrix} \boldsymbol{R}_u \\ \boldsymbol{R}_l \end{bmatrix}^{(k)}, \tag{C.23}$$

where the block matrices are obtained via element-by-element assembly of the individual nodal contributions to the Jacobian:

$$\boldsymbol{K}_{ab} = \frac{\partial \boldsymbol{R}_{u,a}}{\partial \boldsymbol{U}_b} = \int_\Omega \boldsymbol{B}_a^T \mathbf{D} \boldsymbol{B}_b d\Omega, \tag{C.24}$$

$$\boldsymbol{C}^T_{a\bar{b}} = \frac{\partial \boldsymbol{R}_{u,a}}{\partial \boldsymbol{L}_{\bar{b}}} = \int_{\Gamma_{f+}} \boldsymbol{\eta}_a^T \boldsymbol{\eta}_{\bar{b}} d\Gamma - \int_{\Gamma_{f-}} \boldsymbol{\eta}_a^T \boldsymbol{\eta}_{\bar{b}} d\Gamma. \tag{C.25}$$

Matrix $\boldsymbol{C}$ is the part of the Jacobian associated with the slip constraint, Eq. (C.17), and consists of direction cosine matrices to convert from the global coordinate system to the fault coordinate system (vice versa for $\boldsymbol{C}^T$). Note that for a linear elastic material with time-independent material properties and boundary conditions, the Jacobian matrix does not change with time, although the residuals may change due to coupling with the flow and due to fault slip. This is a saddle-point problem. Custom preconditioners are required to solve the linear system efficiently using the Portable, Extensible Toolkit for Scientific Computation (PETSc) [95] multigrid preconditioner for the elasticity submatrix in conjunction with a custom fault preconditioner for the Lagrange multiplier submatrix [56, 57].

Appendix C.3. Two-grid operators

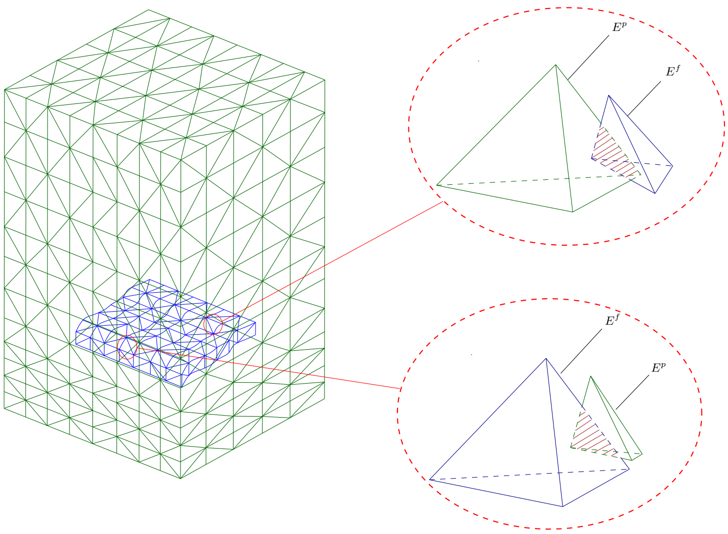

Figure C.11: Depiction of couple of intersecting flow-geomechanics element pairs. We refer to the flow element as E^f and geomechanics element as E^p. Depiction is to reiterate the point that there is no restriction of whether the flow or geomechanics element needs to be smaller than the other

The basic idea of the two-grid approach is to transfer pore pressures from the flow domain to the geomechanics domain and conversely transfer volumetric strain from the geomechanical domain to the flow domain. The transfered pore pressure at every geomechanics element is a volume average of the pore pressures at the flow elements interacting with the geomechanics element. Likewise, the transfered volumetric strain at each flow element is a volume average of the volumetric strains at the geomechanics elements interacting with the flow element. The global two-grid operators are constructed in the pre-processing step by applying a local two-grid procedure to each pair of intersecting finite elements depicted in Fig. C.11. The relationship between the flow-geomechanics element pair is obtained by determining the barycentric coordinates of the vertices of the flow element with respect to the geomechanics element and vice versa as explained in Algorithm 1.

Algorithm 1 Determining the relationship between flow-geomechanics element pairs

```
for Loop over all geomechanics elements do
    for Loop over all flow elements do
        count1 ← 0
        for Loop over four vertices of flow element do
            if Vertex inside geomechanics element then        ▷ Invoke barycentric coordinates
                count1 ← count1 + 1
        if count1!=0 then
            Flow to geomechanics projection operator ← Meas(E^f)
            Geomechanics to flow projection operator ← Meas(E^p)
        count2 ← 0
        for Loop over four vertices of geomechanics element do
            if Vertex inside flow element then                ▷ Invoke barycentric coordinates
                count2 ← count2 + 1
        if count2!=0 then
            Flow to geomechanics projection operator ← Meas(E^f)
            Geomechanics to flow projection operator ← Meas(E^p)
```

References

[1] Traci Rodosta, William Aljoe, Grant Bromhal, and Darin Damiani. U.s. doe regional carbon sequestration partnership initiative: New insights and lessons learned. *Energy Procedia*, 114:5580–5592, 2017.

[2] Robert Balch, Brian McPherson, et al. Integrating enhanced oil recovery and carbon capture and storage projects: a case study at farnsworth field, texas. In *SPE Western Regional Meeting*. Society of Petroleum Engineers, 2016.

[3] National Research Council et al. *Induced seismicity potential in energy technologies*. National Academies Press, 2013.

[4] M. D. Zoback and S. M. Gorelick. Earthquake triggering and large-scale geologic storage of carbon dioxide. *Proc. Natl. Acad. Sci. U.S.A.*, 109:10164–10168, 2012.

[5] M. L. Szulczewski, C. W. MacMinn, H. J. Herzog, and R. Juanes. Lifetime of carbon capture and storage as a climate-change mitigation technology. *Proc. Natl. Acad. Sci. U.S.A.*, 109(14):5185–5189, 2012.

[6] R. Juanes, B. H. Hager, and H. J. Herzog. No geologic evidence that seismicity causes fault leakage that would render large-scale carbon capture and storage unsuccessful. *Proc. Natl. Acad. Sci. U.S.A.*, 109(52):E3623, 2012.

[7] M. D. Zoback and S. M. Gorelick. Reply to Juanes et al.: Evidence that earthquake triggering could render long-term carbon storage unsuccessful in many regions. *Proc. Natl. Acad. Sci. U.S.A.*, 109(52):E3624, 2012.

[8] Matthias Preisig and Jean H Prévost. Coupled multi-phase thermo-poromechanical effects. case study: Co2 injection at in salah, algeria. *International Journal of Greenhouse Gas Control*, 5(4):1055–1064, 2011.

[9] J Rutqvist, J Birkholzer, F Cappa, and C-F Tsang. Estimating maximum sustainable injection pressure during geological sequestration of co2 using coupled fluid flow and geomechanical fault-slip analysis. *Energy Conversion and Management*, 48(6):1798–1807, 2007.

[10] J Rutqvist, JT Birkholzer, and Chin-Fu Tsang. Coupled reservoir–geomechanical analysis of the potential for tensile and shear failure associated with co2 injection in multilayered reservoir–caprock systems. *International Journal of Rock Mechanics and Mining Sciences*, 45(2):132–143, 2008.

[11] Jürgen E Streit and Richard R Hillis. Estimating fault stability and sustainable fluid pressures for underground storage of co2 in porous rock. *Energy*, 29(9-10):1445–1456, 2004.

[12] Pietro Teatini, Nicola Castelletto, and Giuseppe Gambolati. 3d geomechanical modeling for co2 geological storage in faulted formations. a case study in an offshore northern adriatic reservoir, italy. *International Journal of Greenhouse Gas Control*, 22:63–76, 2014.

[13] JP Verdon, J-M Kendall, DJ White, and DA Angus. Linking microseismic event observations with geomechanical models to minimise the risks of storing co2 in geological formations. *Earth and Planetary Science Letters*, 305(1-2):143–152, 2011.

[14] Víctor Vilarrasa, Jesus Carrera, Sebastià Olivella, Jonny Rutqvist, and Lyesse Laloui. Induced seismicity in geologic carbon storage. *Solid Earth*, 10(3):871–892, 2019.

[15] Schlumberger GeoQuest. Eclipse reference manual. *Schlumberger, Houston, Texas*, 2014.

[16] S Cmg. Advanced processes & thermal reservoir simulator, user's guide, 2018.

[17] Odd Andersen, Halvor MøII Nilsen, Xavier Raynaud, et al. Coupled geomechanics and flow simulation on corner-point and polyhedral grids. In *SPE Reservoir Simulation Conference*. Society of Petroleum Engineers, 2017.

[18] Firas H Melaih, Ali A Alturki, Razen M Al-Harbi, and Majdi A Baddourah. Applications of computational geometry for automatic transformation to unstructured reservoir gridding. In *82nd EAGE Annual Conference & Exhibition*, volume 1, pages 1–12. European Association of Geoscientists & Engineers, 2020.

[19] Emmanuel J Gringarten, Mohamed Aymen Haouesse, Guven Burc Arpat, Long X Nghiem, et al. Advantages of using vertical stair step faults in reservoir grids for flow simulation. In *SPE Reservoir Simulation Symposium*. Society of Petroleum Engineers, 2009.

[20] Abdulrahman Bubshait, Birendra Jha, et al. A novel meshing routine for modeling reservoirs with multiple curved and intersecting faults in coupled flow-geomechanical dual 3d grids. In *SPE Western Regional Meeting*. Society of Petroleum Engineers, 2019.

[21] Saumik Dana, Xiaoxi Zhao, and Birendra Jha. Two-grid method on unstructured tetrahedra: Applying computational geometry to staggered solution of coupled flow and mechanics problems. *arXiv preprint arXiv:2102.04455*, 2021.

[22] Birendra Jha and Ruben Juanes. Coupled multiphase flow and poromechanics: A computational model of pore pressure effects on fault slip and earthquake triggering. *Water Resources Research*, 50(5):3776–3808, 2014.

[23] J. Kim, H.A. Tchelepi, and R. Juanes. Stability, accuracy and efficiency of sequential methods for coupled flow and geomechanics. *SPE Journal*, 16(2):249–262, 2011.

[24] A. Mikelić and M.F. Wheeler. Convergence of iterative coupling for coupled flow and geomechanics. *Computational Geosciences*, 17(3):455–461, 2013.

[25] A. Mikelić, B. Wang, and M. F. Wheeler. Numerical convergence study of iterative coupling for coupled flow and geomechanics. *Computational Geosciences*, 18(3):325–341, 2014.

[26] N. Castelletto, J. A. White, and H. A. Tchelepi. Accuracy and convergence properties of the fixed-stress iterative solution of two-way coupled poromechanics. *International Journal for Numerical and Analytical Methods in Geomechanics*, 39(14):1593–1618, 2015.

[27] J. A. White, N. Castelletto, and H. A. Tchelepi. Block-partitioned solvers for coupled poromechanics: A unified framework. *Computer Methods in Applied Mechanics and Engineering*, 303:55–74, 2016.

[28] N. Castelletto, J. A. White, and M. Ferronato. Scalable algorithms for three-field mixed finite element coupled poromechanics. *Journal of Computational Physics*, 327:894–918, 2016.

[29] S. Dana and M. F. Wheeler. Convergence analysis of fixed stress split iterative scheme for anisotropic poroelasticity with tensor biot parameter. *Computational Geosciences*, 22(5):1219–1230, 2018.

[30] S. Dana and M. F. Wheeler. Convergence analysis of two-grid fixed stress split iterative scheme for coupled flow and deformation in heterogeneous poroelastic media. *Computer Methods in Applied Mechanics and Engineering*, 341:788–806, 2018.

[31] Saumik Dana, Joel Ita, and Mary F Wheeler. The correspondence between voigt and reuss bounds and the decoupling constraint in a two-grid staggered algorithm for consolidation in heterogeneous porous media. *Multiscale Modeling & Simulation*, 18(1):221–239, 2020.

[32] T. Almani, K. Kumar, A. Dogru, G. Singh, and M. F. Wheeler. Convergence analysis of multirate fixed-stress split iterative schemes for coupling flow with geomechanics. *Computer Methods in Applied Mechanics and Engineering*, 311:180–207, 2016.

[33] T. Almani, K. Kumar, and M. F. Wheeler. Convergence and error analysis of fully discrete iterative coupling schemes for coupling flow with geomechanics. *Computational Geosciences*, 2017.

[34] Jakub Wiktor Both, Kundan Kumar, Jan Martin Nordbotten, and Florin Adrian Radu. Anderson accelerated fixed-stress splitting schemes for consolidation of unsaturated porous media. *Computers and Mathematics with Applications*, 77(6):1479 – 1502, 2019. 7th International Conference on Advanced Computational Methods in Engineering (ACOMEN 2017).

[35] Joshua A. White, Nicola Castelletto, Sergey Klevtsov, Quan M. Bui, Daniel Osei-Kuffuor, and Hamdi A. Tchelepi. A two-stage preconditioner for multiphase poromechanics in reservoir simulation. *Computer Methods in Applied Mechanics and Engineering*, 357:112575, 2019.

[36] Manuel Borregales, Kundan Kumar, Florin Adrian Radu, Carmen Rodrigo, and Francisco José Gaspar. A partially parallel-in-time fixed-stress splitting method for biot's consolidation model. *Computers and Mathematics with Applications*, 77(6):1466 – 1478, 2019. 7th International Conference on Advanced Computational Methods in Engineering (ACOMEN 2017).

[37] Erlend Storvik, Jakub W. Both, Kundan Kumar, Jan M. Nordbotten, and Florin A. Radu. On the optimization of the fixed-stress splitting for biot's equations. *International Journal for Numerical Methods in Engineering*, page nme.6130, 2019.

[38] Florin Adrian Radu, Jan Martin Nordbotten, Iuliu Sorin Pop, and Kundan Kumar. A robust linearization scheme for finite volume based discretizations for simulation of two-phase flow in porous media. *Journal of Computational and Applied Mathematics*, 289:134 – 141, 2015.

[39] Elyes Ahmed, Jan Martin Nordbotten, and Florin Adrian Radu. Adaptive asynchronous time-stepping, stopping criteria, and a posteriori error estimates for fixed-stress iterative schemes for coupled poromechanics problems. *Journal of Computational and Applied Mathematics*, 364:112312, 2020.

[40] Xueying Lu and Mary F. Wheeler. Three-way coupling of multiphase flow and poromechanics in porous media. *Journal of Computational Physics*, 401:109053, 2020.

[41] Saumik Dana and Mary F Wheeler. Design of convergence criterion for fixed stress split iterative scheme for small strain anisotropic poroelastoplasticity coupled with single phase flow. *arXiv preprint arXiv:1912.06476*, 2019.

[42] Saumik Dana. System of equations and staggered solution algorithm for immiscible two-phase flow coupled with linear poromechanics. *arXiv preprint arXiv:1912.04703*, 2019.

[43] Thomas Dewers, Peter Eichhubl, Ben Ganis, Steven Gomez, Jason Heath, Mohamad Jammoul, Peter Kobos, Ruijie Liu, Jonathan Major, Ed Matteo, Pania Newell, Alex Rinehart, Steven Sobolik, John Stormont, Mahmoud Reda Taha, Mary Wheeler, and Deandra White. Heterogeneity, pore pressure, and injectate chemistry: Control measures for geologic carbon storage. *International Journal of Greenhouse Gas Control*, 68:203 – 215, 2018.

[44] Mohamad Jammoul, Benjamin Ganis, and Mary Wheeler. General semi-structured discretization for flow and geomechanics on diffusive fracture networks. In *SPE Reservoir Simulation Conference*. Society of Petroleum Engineers, 2019.

[45] Mary F. Wheeler, Ivan Yotov, Benjamin Ganis, Gergina Pencheva, Omar Al Hinai, Sangyun Lee, Baehyun Min, Jing Ping, Gurpreet Singh, Tameem Almani, Saumik Dana, Mohammad Jammoul, Deandra White, Paolo Zunino, Ilona Ambartsumyan, Eldar Khattatov, Truong Nguyen, Pu Song, Roxana Tanase, ChangQing Wang, and Rana Zakerzadeh. Multiscale modeling and simulation of multiphase flow in porous media coupled with geomechanics (final report). *https://www.osti.gov/biblio/1509810*, 4 2019.

[46] S. Dana. *Addressing challenges in modeling of coupled flow and poromechanics in deep subsurface reservoirs*. PhD thesis, The University of Texas at Austin, 2018.

[47] T Kadeethum, S Lee, F Ballarin, J Choo, and HM Nick. A locally conservative mixed finite element framework for coupled hydro-mechanical-chemical processes in heterogeneous porous media. *arXiv preprint arXiv:2010.04994*, 2020.

[48] Yongzan Liu, Lijun Liu, Juliana Y Leung, Kan Wu, and George Moridis. Coupled flow/geomechanics modeling of interfracture water injection to enhance oil recovery in tight reservoirs. *SPE Journal*, 26(01):1–21, 2021.

[49] Yongzan Liu, Lijun Liu, Juliana Y Leung, and George J Moridis. Sequentially coupled flow and geomechanical simulation with a discrete fracture model for analyzing fracturing fluid recovery and distribution in fractured ultra-low permeability gas reservoirs. *Journal of Petroleum*

Science and Engineering, 189:107042, 2020.
[50] Lijun Liu, Yongzan Liu, Jun Yao, Zhaoqin Huang, et al. Efficient coupled multiphase-flow and geomechanics modeling of well performance and stress evolution in shale-gas reservoirs considering dynamic fracture properties. *SPE Journal*, 2020.
[51] Omar Duran, Manouchehr Sanei, Philippe RB Devloo, and Erick SR Santos. An enhanced sequential fully implicit scheme for reservoir geomechanics. *Computational Geosciences*, 24(4):1557–1587, 2020.
[52] Sebastian BM Bosma, Sergey Klevtsov, Olav Møyner, and Nicola Castelletto. Enhanced multiscale restriction-smoothed basis (msrsb) preconditioning with applications to porous media flow and geomechanics. *Journal of Computational Physics*, 428:109934, 2021.
[53] J. Mandel. Consolidation des sols (étude mathématique)*. *Géotechnique*, 3(7):287–299, 1953.
[54] Y. Abousleiman, A. H. D. Cheng, L. Cui, E. Detournay, and J. C. Roegiers. Mandel's problem revisited. *Géotechnique*, 46(2):187–195, 1996.
[55] Knut-Andreas Lie. *An introduction to reservoir simulation using MATLAB/GNU Octave: User guide for the MATLAB Reservoir Simulation Toolbox (MRST)*. Cambridge University Press, 2019.
[56] B Aagaard, S Kientz, M Knepley, L Strand, and C Williams. Pylith user manual: version 2.1. 0. *Davis, CA: Computational Infrastructure of Geodynamics*, 2013.
[57] Brad T Aagaard, Matthew G Knepley, and Charles A Williams. A domain decomposition approach to implementing fault slip in finite-element models of quasi-static and dynamic crustal deformation. *Journal of Geophysical Research: Solid Earth*, 118(6):3059–3079, 2013.
[58] Ted D Blacker, William J Bohnhoff, and Tony L Edwards. Cubit mesh generation environment. volume 1: Users manual. Technical report, Sandia National Labs., Albuquerque, NM (United States), 1994.
[59] George El-kaseeh, Robert Will, Robert Balch, and Reid Grigg. Multi-scale seismic measurements for co2 monitoring in an eor/ccus project. *Energy Procedia*, 114:3656–3670, 2017.
[60] Xiaoxi Zhao and Birendra Jha. Role of well operations and multiphase geomechanics in controlling fault stability during co2 storage and enhanced oil recovery. *Journal of Geophysical Research: Solid Earth*, 124(7):6359–6375, 2019.
[61] Mark D White, RP Esser, BP McPherson, RS Balch, N Liu, PE Rose, L Garcia, and W Ampomah. Interpretation of tracer experiments on inverted five-spot well-patterns within the western half of the farnsworth unit oil field. *Energy Procedia*, 114:7070–7095, 2017.
[62] Ashley C Hutton. *Geophysical modeling and structural interpretation of a 3D reflection seismic survey in Farnsworth Unit, TX*. New Mexico Institute of Mining and Technology, 2015.
[63] Robert Balch, Robert Will*, George El-Kaseeh, Reid Grigg, Ashley Hutton, and Paige Czoski. Integrating multi-scale seismic measurements for eor/ccus. In *SEG Technical Program Expanded Abstracts 2015*, pages 2837–2841. Society of Exploration Geophysicists, 2015.
[64] Sara R Gallagher. *Depositional and diagenetic controls on reservoir heterogeneity: upper morrow sandstone, Farnsworth unit, Ochiltree county, Texas*. PhD thesis, Citeseer, 2014.
[65] Dylan Rose-Coss, William Wampomah, Ashley C Hutton, Evan Gragg, Peter Mozley, Robert S Balch, and Reid Grigg. Geologic characterization for co 2-eor simulation: A case study of the farnsworth unit, anadarko basin, texas. In *AAPG Annual Convention and Exhibition*, 2015.
[66] W Ampomah, RS Balch, D Ross-Coss, A Hutton, M Cather, RA Will, et al. An integrated approach for characterizing a sandstone reservoir in the anadarko basin. In *Offshore Technology Conference*. Offshore Technology Conference, 2016.
[67] William Ampomah, Robert Balch, Martha Cather, Dylan Rose-Coss, Zhenxue Dai, Jason Heath, Thomas Dewers, and Peter Mozley. Evaluation of co2 storage mechanisms in co2 enhanced oil recovery sites: Application to morrow sandstone reservoir. *Energy & Fuels*, 30(10):8545–8555, 2016.
[68] K. Aziz and A. Settari. *Petroleum Reservoir Simulation*. Elsevier, London, 1979.
[69] J. Bear. *Dynamics of Fluids in Porous Media*. Wiley, New York, 1972.
[70] O. Coussy. Poromechanics of freezing materials. *J. Mech. Phys. Solids*, 53:1689–1718, 2005.
[71] M. A. Biot. General theory of three-dimensional consolidation. *J. Appl. Phys.*, 12:155–164, 1941.
[72] O. Coussy. *Mechanics of Porous Continua*. John Wiley and Sons, Chichester, England, 1995.
[73] R. W. Lewis and Y. Sukirman. Finite element modelling of three-phase flow in deforming saturated oil reservoirs. *Int. J. Numer. Anal. Methods Geomech.*, 17:577–598, 1993.
[74] O. Coussy, R. Eymard, and T. Lassabatére. Constitutive modeling of unsaturated drying deformable materials. *J. Eng. Mech.*, 124(6):658–557, 1998.
[75] R. W. Lewis and B. A. Schrefler. *The Finite Element Method in the Static and Dynamic deformation and Consolidation of Porous Media*. Wiley, Chichester, England, second edition, 1998.
[76] N. Khalili, F. Geiser, and G. E. Blight. Effective stress in unsaturated soils, a review with new evidence. *Int. J. Geomech.*, 4:115–126, 2004.
[77] M. Nuth and L. Laloui. Effective stress concept in unsaturated soils: Clarification and validation of a unified framework. *Int. J. Numer. Anal. Methods Geomech.*, 32:771–801, 2008.
[78] W. G. Gray and B. A. Schrefler. Thermodynamic approach to effective stress in partially saturated porous media. *Eur. J. Mech.-A*, 20:521–538, 2001.
[79] O. Coussy, P. Dangla, T. Lassabatére, and V. Baroghel-Bouny. The equivalent pore pressure and the swelling and shrinkage of cement-based materials. *Mater. Struct.*, 37:15–20, 2004.
[80] I. Vlahinic, H. M. Jennings, J. E. Andrade, and J. J. Thomas. A novel and general form of effective stress in a partially saturated porous material: The influence of microstructure. *Mech. Mater.*, 43:25–35, 2011.
[81] E. Nikooee, G. Habibagahi, S. M. Hassanizadeh, and A. Ghahramani. Effective stress in unsaturated soils: A thermodynamic approach based on the interfacial energy and hydromechanical coupling. *Transp. Porous Med.*, 96:369–396, 2013.
[82] J. Kim, H. A. Tchelepi, and R. Juanes. Rigorous coupling of geomechanics and multiphase flow with strong capillarity. *Soc. Pet. Eng. J.*, 18(6):1123–1139, 2013.
[83] O. Coussy. *Poromechanics*. John Wiley and Sons, Chichester, England, 2004.
[84] M. Muskat. *Physical Principles of Oil Production*. McGraw-Hill, New York, 1949.
[85] Saumik Dana and Mary F Wheeler. Augmented lagrangian for treatment of hanging nodes in hexahedral meshes. *arXiv preprint arXiv:1809.04031*, 2018.

[86] Ajay B Harish and Peter Wriggers. Modeling of two-body abrasive wear of filled elastomers as a contact-induced fracture process. *Tribology International*, 138:16–31, 2019.

[87] Christian Weißenfels, Ajay B Harish, and Peter Wriggers. Strategies to apply soil models directly as friction laws in soil structure interactions. In *Holistic Simulation of Geotechnical Installation Processes*, pages 216–236. Springer, 2017.

[88] J. C. Jaeger and N. G. W. Cook. *Fundamentals of Rock Mechanics*. Chapman and Hall, London, 1979.

[89] R. J. LeVeque. *Finite Volume Methods for Hyperbolic Problems*. Cambridge University Press, UK, 2002.

[90] D. Gunasekera, P. Childs, J. Herring, and J. Cox. A multi-point flux discretization scheme for general polyhedral grids. In *6th SPE International Oil and Gas Conference and Exhibition*, Beijing, 1998.

[91] I. Aavatsmark. An introduction to multipoint flux approximations for quadrilateral grids. *Comput. Geosci.*, 6:405–432, 2002.

[92] K Stüben and T Clees. Samg user's manual v. 22c. *Fraunhofer Institute SCAI, Schloss Birlinghoven, Sankt Augustin, Germany*, 2005.

[93] H Pan and H Cao. User manual for general purpose research simulator, 2010.

[94] T. J. R. Hughes. *The Finite Element Method: Linear Static and Dynamic Finite Element Analysis*. Prentice-Hall, Englewood Cliffs, NJ, 1987.

[95] Satish Balay, Shrirang Abhyankar, Mark Adams, Jed Brown, Peter Brune, Kris Buschelman, Lisandro Dalcin, Alp Dener, Victor Eijkhout, W Gropp, et al. Petsc users manual. *See http://www. mcs. anl. gov/petsc*, 2019.